Low-Loss Photonic Integrated Elements Based on Bound Bloch Surface Wave in the Continuum

Haoqi Luo,[1,2] Xi Tang,[1,2] Yonghua Lu,[1,2,*] and Pei Wang[1,2]

[1] *Department of Optics and Optical Engineering, University of Science and Technology of China, Hefei, Anhui 230026, China*

[2] *Advanced Laser Technology Laboratory of Anhui Province, Hefei, Anhui 230026, China*

(Received 9 April 2021; revised 30 June 2021; accepted 9 July 2021; published 28 July 2021)

A Bloch surface wave (BSW) confined at the surface of a truncated dielectric multilayer is a low-loss platform for chip-scale photonic integration. The guided BSW in a dielectric ridge is confined by the photonic band gap vertically, yet couples into the continuum modes of the multilayered substrate horizontally. We demonstrate that a low-loss BSW waveguide can be realized with the quasibound BSW modes in the continuum by engineering the geometric parameters, due to the destructive interference of multiple leakage channels in the multilayered substrate. In addition, a high-Q BSW resonator is obtained by optimizing the geometric parameter of the multilayered substrate, which provides an alternative way to realize ultrasmall resonators with a high-Q factor. The photonic integrated circuits on a low-loss BSW platform can be utilized for optical communications, enhancing light-matter interactions, and nonlinear optical applications.

DOI: 10.1103/PhysRevApplied.16.014064

I. INTRODUCTION

In recent years, photonic integrated circuits (PICs) have attracted a great deal of attention for their potential applications in lasing [1,2], nonlinear optics [3,4], and optical telecommunication [5,6]. The silicon-on-insulator structure [7] is the most widely used platform for PICs, in which light is confined by total internal reflection (TIR). PICs can also be developed based on electromagnetic surface waves that localize at the interface between the substrate and surrounding medium [8]. Surface-plasmon polaritons (SPPs) [9] on metallic film have been regarded as a potential platform for PICs, but suffer from the intrinsic loss of metal, which restricts the scale of integration. As the dielectric analogue of SPPs, Bloch surface waves (BSWs) [10,11] confine electromagnetic waves at the topmost layer of a truncated all-dielectric multilayer through the mechanism of TIR and the photonic band gap (PBG) of a one-dimensional photonic crystal (1DPC). Due to hybrid confinement, BSWs show surface field enhancement [12], which can help to enhance light-matter interactions [13] and realize high-precision optical sensing [14]. Since BSWs circumvent the intrinsic metallic loss and have a broad range of working wavelengths, it is widely anticipated that low-loss PICs could be constructed based on the BSW platform. However, experimental results for BSW waveguides and resonators have not presented any dramatic reduction of the propagation loss to date [15–17].

The localization of light based on the generalized TIR mechanism could be equivalent to particle confinement in a potential well in quantum mechanics due to the similarity of the Schrödinger equation and the Helmholtz equation [18]. When the generalized TIR condition is broken, light passes through the boundary and then propagates to infinity, corresponding to the continuum mode, the eigenenergy of which is above the potential well, and the wave function spreads to infinity. Nevertheless, light can be confined with an infinite lifetime in some properly engineered structures, even though the TIR condition is not met. This phenomenon relies on a method for light confinement called bound states in the continuum (BIC) [19], which was proposed by von Neumann and Wigner in 1929 [20]. Recently, various types of BIC-based optical waveguide structures have been developed, including a symmetry-protected BIC [21], a Fabry-Perot BIC [22,23], a Friedrich-Wintgen BIC [24,25], and a single-resonance BIC [26,27]. The first originates from the incompatible symmetry of the bound and continuum modes. The last three are attributed to destructive interference between multiple continuum modes.

Here, we investigate the lateral leakage loss arising from the coupling between the bound surface mode and the continuums within the truncated 1DPC. We demonstrate that the leakage loss can be greatly inhibited by the BIC mechanism to diminish the propagation loss of

*yhlu@ustc.edu.cn

a BSW waveguide and resonator. First, the Bloch modes of a finite dielectric multilayer are discussed by solving the transfer-matrix problem [28]. Second, a waveguide on a single-binary-layer substrate is analyzed, and leakage loss can be eliminated by elaborately designing the device to realize the BIC state for the guided mode. Third, the leakage loss of a BSW waveguide on the truncated 1DPC is investigated by considering the destructive interference of multiple leakage channels, and the quasi-BIC guided mode is obtained by engineering the geometric parameters. Finally, a high-Q BSW resonator is also introduced by fabricating a disk on top of the multilayered substrate, and the Q factor is optimized by comprehensive consideration of bending loss and leakage loss.

II. BLOCH MODE OF ALTERNATING MULTILAYER

Figure 1(a) illustrates a schematic of the truncated photonic multilayer structure. The periodic binary photonic multilayer is composed of N pairs of alternating SiO_2 layers (refractive index $n_a = 1.46$) with thickness d_a and Si_3N_4 layers ($n_b = 2.14$) with thickness d_b. The multilayer is deposited on SiO_2 substrate and covered by an additional Si_3N_4 film with fixed thickness of $h = 90$ nm. The device is surrounded by air. The electromagnetic wave in the multilayer propagating along the y axis can be expressed as $\mathbf{E}(z)e^{-in_{\text{eff}}k_0 y}$ for the electric field and $\mathbf{H}(z)e^{-in_{\text{eff}}k_0 y}$ for the magnetic field, in which n_{eff} denotes the effective refractive index. Thus, polarization of the eigenmodes can be classified as TE modes with **E** parallel to the x axis and TM modes with **H** parallel to the x axis. In the following, we focus on a working wavelength of $\lambda = 532$ nm and analyze the eigenmodes by solving the electromagnetic eigenvalue problem via the transfer-matrix method (TMM). Without loss of generality, the effective refractive index is calculated under the assumption of $d_a = 250$ nm.

We start the investigation from the simplest multilayer structure of single alternating layers ($N = 1$) covered by the additional Si_3N_4 film. We term the electromagnetic mode spreading over the multilayer as an internal mode and the one localized by the topmost layer as the surface mode. As shown in Fig. 1(b), the effective refractive index of internal modes (dotted lines) strongly depends on thickness d_b, while the effective refractive index of the TE surface mode (black solid line) remains almost constant. The anticrossing behavior when the effective refractive indices of TE internal and surface modes approach each other indicates strong coupling between them. The dispersion curve of the TE surface mode crossing directly over that of the TM internal mode implies no coupling between the two modes because of the polarization orthogonality. Another important thing that should be noted is the different parity of the TE surface mode when d_b is smaller or larger than the resonant thickness (the anticrossing point). The electric field of the TE surface mode is even for $d_b = 65$ nm [left inset of Fig. 1(b)] and odd for $d_b = 85$ nm [right inset of Fig. 1(b)].

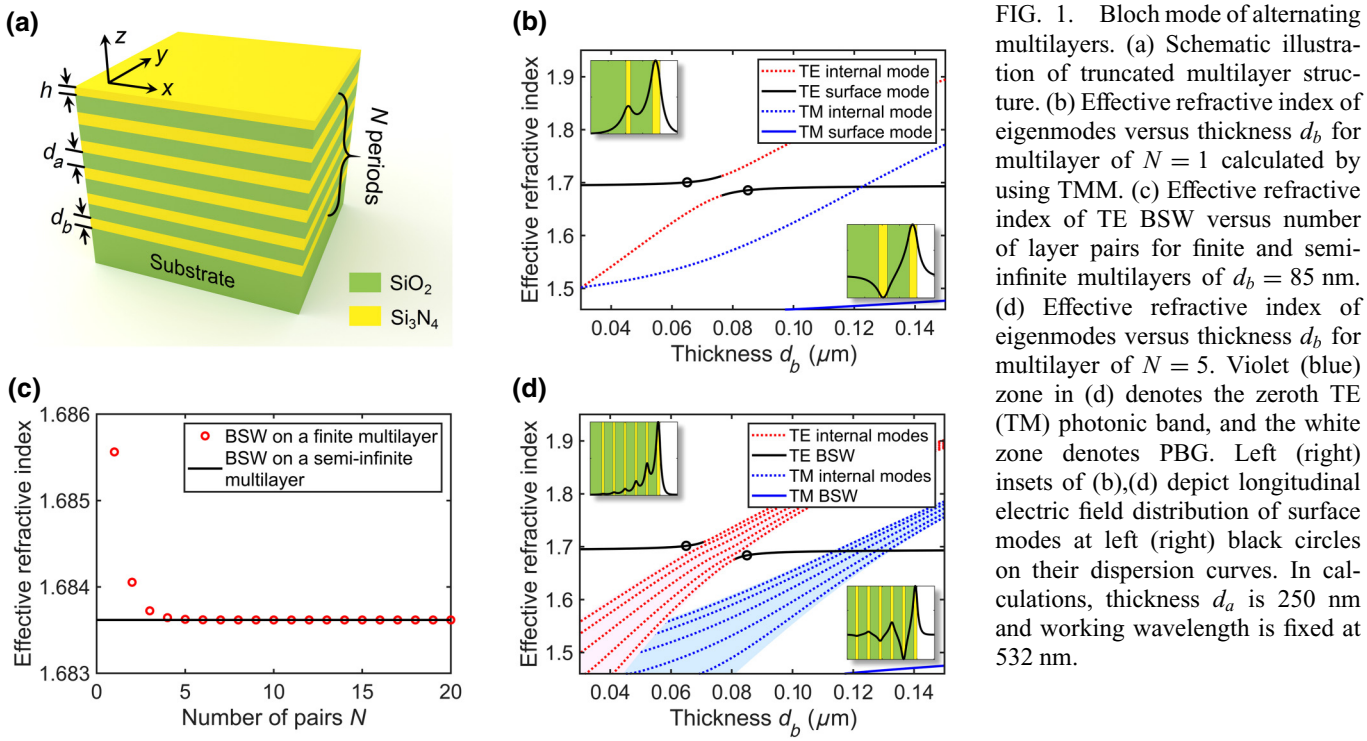

FIG. 1. Bloch mode of alternating multilayers. (a) Schematic illustration of truncated multilayer structure. (b) Effective refractive index of eigenmodes versus thickness d_b for multilayer of $N = 1$ calculated by using TMM. (c) Effective refractive index of TE BSW versus number of layer pairs for finite and semi-infinite multilayers of $d_b = 85$ nm. (d) Effective refractive index of eigenmodes versus thickness d_b for multilayer of $N = 5$. Violet (blue) zone in (d) denotes the zeroth TE (TM) photonic band, and the white zone denotes PBG. Left (right) insets of (b),(d) depict longitudinal electric field distribution of surface modes at left (right) black circles on their dispersion curves. In calculations, thickness d_a is 250 nm and working wavelength is fixed at 532 nm.

The dispersion relation of internal modes develops into the photonic band structure for the periodic binary multilayer with infinite stacking pairs ($N \to \infty$), which is also known as the 1DPC. According to the Bloch theorem [10], the electric field of the Bloch mode is periodic, as follows:

$$E(z + \Lambda) = e^{iK_{\mathrm{BW}}\Lambda}E(z). \quad (1)$$

Here, the period is defined as $\Lambda = d_a + d_b$ and K_{BW} denotes the Bloch wave vector. Instead of a real Bloch wave vector for a propagating Bloch wave in the photonic bands, the Bloch wave in the PBGs is evanescent with a complex wave vector, $K_{\mathrm{BW}} = \alpha\pi/\Lambda + iK_{\mathrm{BW}}^{\mathrm{Im}}$, where integer α is the PBG index. Although an ideal 1DPC has infinite pairs of alternating layers, the real 1DPC sample is commonly fabricated by depositing finite layers alternatingly on a substrate. Figure 1(c) presents the effective refractive indices of BSWs in the finite (red circles) and semi-infinite (black solid line) multilayers with $d_b = 85$ nm. Fortunately, we find that the effective refractive index of the BSW in the finite multilayer quickly approaches that of a semi-infinite multilayer while increasing the number of stacking pairs. It is reasonable to neglect the difference between the BSW mode in the semifinite multilayer and that in the finite multilayer with $N = 5$; this structure is utilized in the following calculations.

Figure 1(d) shows the effective refractive index of TE and TM Bloch modes in the finite multilayer ($N = 5$) as a function of thickness d_b. The violet (blue) zone denotes the zeroth TE (TM) photonic band, and the white zones above and below it denote the zeroth and first TE (TM) PBGs, respectively. The dispersion curve of the BSW (black solid line) is located in the PBGs and above the light line in air ($n_{\mathrm{eff}} > 1$), implying that the electromagnetic field is evanescent in both the multilayer and air. At the edges of the TE photonic band, strong coupling between the TE BSW and photonic band leads to anticrossing. The dispersion line of the TE BSW crosses the TM photonic band without interaction due to polarization orthogonality between them. The electric field of the TE BSW decays in adjacent layer pairs by a factor of $(-1)^{\alpha}e^{-K_{\mathrm{BW}}^{\mathrm{Im}}\Lambda}$, which indicates that parity of the BSW field in adjacent layer pairs is determined by the PBG index. As presented in the left and right insets of Fig. 1(d), the electric field distribution of the TE BSW in adjacent layer pairs is even for $d_b = 65$ nm (zeroth TE PBG, $\alpha = 0$) and odd for $d_b = 85$ nm (first TE PBG, $\alpha = 1$), indicating that there is a π-phase reversal between the fields in adjacent layer pairs for the TE BSW in the first TE PBG [right inset of Fig. 1(d)] and no phase difference for that in the zeroth TE PBG [left inset of Fig. 1(d)]. In the above discussion, we investigate only the eigenmodes under variation of thickness d_b. Actually, thickness d_a also has an effect on the eigenmodes and band structure [10], but it does not make the dispersion line of the BSW cross over the photonic bands, which does not contribute to the following discussion.

III. WAVEGUIDE BASED ON SINGLE BINARY LAYER

A. Eigenmodes of waveguide on single binary layer

A ridge waveguide on a substrate of a single binary layer is first investigated to illustrate how the BIC mechanism inhibits the leakage loss of the BSW-guided mode. Figure 2(a) illustrates the schematic waveguide structure: a Si_3N_4 ridge with width w and fixed thickness $h = 90$ nm is deposited on a single binary layer ($N = 1$). The cross section of the waveguide structure can be divided into two different regions: region $R2$ is covered by the Si_3N_4 ridge and region $R1$ is without the additional top Si_3N_4 layer. Figure 2(b) shows the effective-refractive-index distribution for light propagating along the ridge waveguide on the single binary layer with $d_a = 250$ nm and $d_b = 100$ nm. The effective refractive indices of the internal modes are calculated to be $n_{R1,\mathrm{int,TE(TM)}} = 1.777(1.619)$ in region $R1$ and $n_{R2,\mathrm{int,TE(TM)}} = 1.778(1.625)$ in region $R2$ for TE (TM) polarization. The TE surface mode exists only in region $R2$ with an effective refractive index of $n_{R2,\mathrm{sur,TE}} = 1.69$. The continuum modes in the x direction for the TE (TM) internal mode is below $n_{R1,\mathrm{int,TE(TM)}}$. The Si_3N_4 ridge induces a different effective refractive index of eigenmodes between regions $R1$ and $R2$, which gives rise to the TE bound surface mode (eigenmode of the waveguide). When the effective refractive index of the bound surface mode is less than that of TE (TM) internal modes, the bound mode lies within the spectrum of the TE (TM) continuum on the x axis. Figure 2(c) shows the normalized electric field distribution of the fundamental TE bound surface mode. Besides the dominant component E_x, the other two components are also nonzero, owing to light confinement in the x direction. Furthermore, it can be observed in Fig. 2(c) that the parity of E_x is even in the x direction while those of E_y and E_z are odd.

B. Lateral leakage of bound surface mode in the TE continuum

As shown in Fig. 2(b), the bound surface mode lies within the TE continuum. Therefore, coupling between the bound surface mode and the TE continuum mode with phase matching could result in significant lateral leakage. To calculate the coupling strength between the bound mode and continuum quantitatively, a variant of the waveguide is first studied in which the binary layer substrate has a finite width s [left inset of Fig. 2(d)]. The coupling strength depends on the width of the substrate, which is analogous to the non-Markovian interaction between the system and finite environment [29]. Because of the finite substrate width, TE continuums are

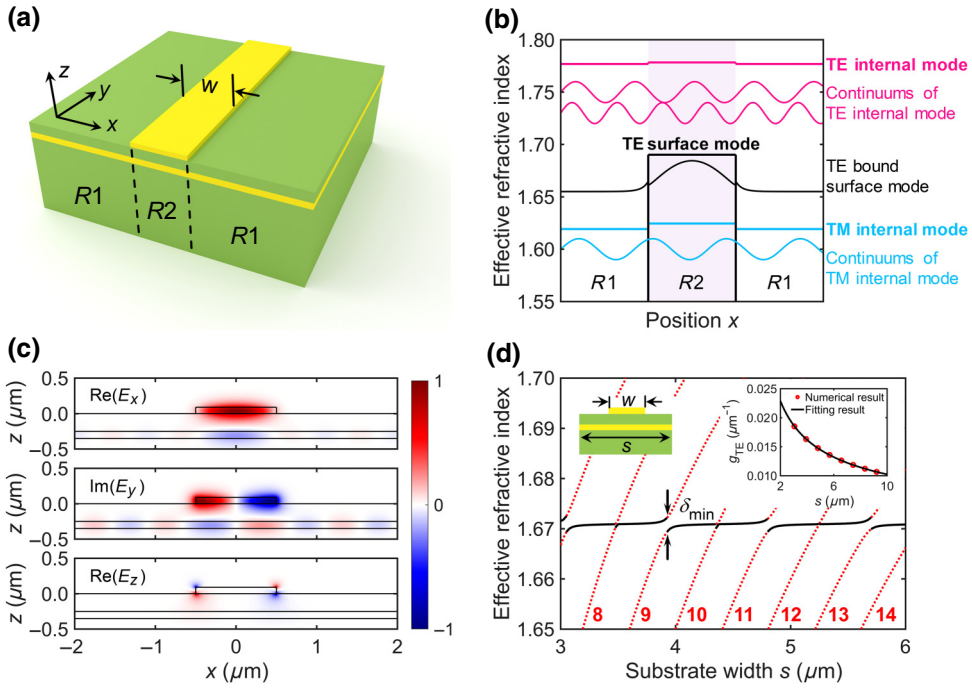

FIG. 2. Eigenmodes in a waveguide based on a single binary layer and coupling between the bound surface mode and the discrete internal mode. (a) Schematic illustration of a waveguide on a substrate of a single binary layer. (b) Effective-refractive-index distribution of eigenmodes propagating along the y axis, where violet and white zones denote regions $R2$ and $R1$, respectively. (c) Electric field distribution of TE bound surface mode. (d) Effective refractive index of TE bound surface mode (black solid line) and TE discrete internal modes (red dotted lines) versus substrate width, s, calculated by FDFD. Left inset of (d) schematically illustrates the waveguide on the finitely wide substrate. Right inset of (d) depicts the coupling strength between the TE bound surface mode and the TE discrete internal mode versus substrate width, s, and the fitting curve of $1/\sqrt{s}$. In calculations, waveguide width, w, is 1 μm, and thicknesses d_a and d_b are fixed at 250 and 100 nm, respectively.

quantized to discrete internal modes under the condition of $\sqrt{n_{R1,\mathrm{int,TE}}^2 - (n_{\mathrm{dis,TE}}^j)^2}\,k_0 s \approx j\pi$, where $n_{\mathrm{dis,TE}}^j$ is the effective refractive index of the jth TE discrete internal mode. Figure 2(d) shows the effective refractive indices of the TE bound surface mode (black solid line) and TE discrete internal modes (red dotted lines) versus substrate width s with waveguide width w fixed at 1 μm, which is calculated by the full-vector finite-difference frequency-domain (FDFD) method (Ansys Lumerical, Inc) [30]. A perfectly matched layer boundary is employed for leakage absorption and loss calculations in the FDFD calculations. Since the horizontal field component, E_x, of the TE bound surface mode is even in the x direction, the bound mode can only couple with the TE discrete internal modes of the same parity due to their nonzero field overlap. The parity of the jth TE discrete internal mode in the x direction is odd (even) when j is even (odd). Hence, the dispersion curves exhibit crossing without interplay for even j and anticrossing for odd j due to coupling when the two modes are near resonance ($n_{\mathrm{bound}} \approx n_{\mathrm{dis,TE}}^j$). The effective-refractive-index difference between the hybrid eigenmodes is $\delta = \sqrt{4(g_{\mathrm{TE}}/k_0)^2 + (n_{\mathrm{bound}} - n_{\mathrm{dis,TE}}^j)^2}$. The coupling strength, g_{TE}, between the bound mode and jth TE discrete internal mode can be obtained by the minimum splitting of mode indices, $g_{\mathrm{TE}} = \delta_{\min} k_0/2$, which is determined by the overlapping integral between the normalized field distribution of the bound surface mode, $\mathbf{E}_{\mathrm{sur}}$, and discrete internal mode, $\mathbf{E}_{\mathrm{int}}$ [29],

$$g_{\mathrm{TE}} = \frac{k_0}{2n_{\mathrm{bound}}}\sqrt{\iint (\mathbf{E}_{\mathrm{sur}})^*(\Delta\varepsilon_{\mathrm{sur}})\cdot\mathbf{E}_{\mathrm{int}}dxdz \iint (\mathbf{E}_{\mathrm{int}})^*(\Delta\varepsilon_{\mathrm{int}})\cdot\mathbf{E}_{\mathrm{sur}}dxdz}. \quad (2)$$

Here, $\Delta\varepsilon_{\mathrm{sur(int)}}$ is the relative permittivity difference caused by the ridge (binary layer). The amplitude of the normalized electric field, $\mathbf{E}_{\mathrm{int}}$, is proportional to $1/\sqrt{s}$, leading to the same dependence of coupling strength, g_{TE}, on the substrate width, s, which is in excellent agreement with the curve fitted by $1/\sqrt{s}$ [right inset of Fig. 2(d)].

The width of the ridge, w, is another critical parameter to determine the coupling strength, g_{TE}. The bound mode dissipates to left-going and right-going TE continuum modes in two channels from both side edges of the waveguide. Considering the phase difference arising from propagation over the waveguide (i.e., $k_{\mathrm{TE},x}w$) and scattering at the side edges (i.e., φ_{TE}) [31], a phase difference of $k_{\mathrm{TE},x}w + \varphi_{\mathrm{TE}}$ is induced between the two channels, where $k_{\mathrm{TE},x} = \sqrt{n_{R1,\mathrm{int,TE}}^2 - n_{\mathrm{bound}}^2}k_0$. Consequently, the coupling strength can be written as

$$g_{\mathrm{TE}} \approx c_{\mathrm{TE}} \frac{|1 + e^{i(k_{\mathrm{TE},x}w + \varphi_{\mathrm{TE}})}|}{2\sqrt{sw^3}}, \tag{3}$$

where c_{TE} is a constant mainly determined by the overlapping integral over variable z, and the factor of $1/\sqrt{w^3}$ stems from field overlap in the x direction [inset of Fig. 3(a)]. Equation (3) illustrates the underlying physics of the BIC mechanism: the coupling strength vanishes when $(k_{\mathrm{TE},x}w + \varphi_{\mathrm{TE}})/\pi$ is odd, corresponding to destructive interference of the two loss channels. Figure 3(a) shows the normalized coupling strength ($\sqrt{s}g_{\mathrm{TE}}$) between the bound mode and 21st TE discrete internal mode, depending on the waveguide width, obtained from FDFD-calculated splitting (red circles). The coupling strength approaches zero at some specific widths because of destructive interference between the continuum modes arising from both side edges of the waveguide. The analytical curve [black solid line in Fig. 3(a)], calculated from Eq. (3), agrees well with the numerical data obtained by FDFD.

For an infinitely wide substrate, lateral leakage of the bound mode into the continuum mode can be calculated by the model of the Markov system-environment interaction [29]. The leakage loss caused by the TE continuum mode

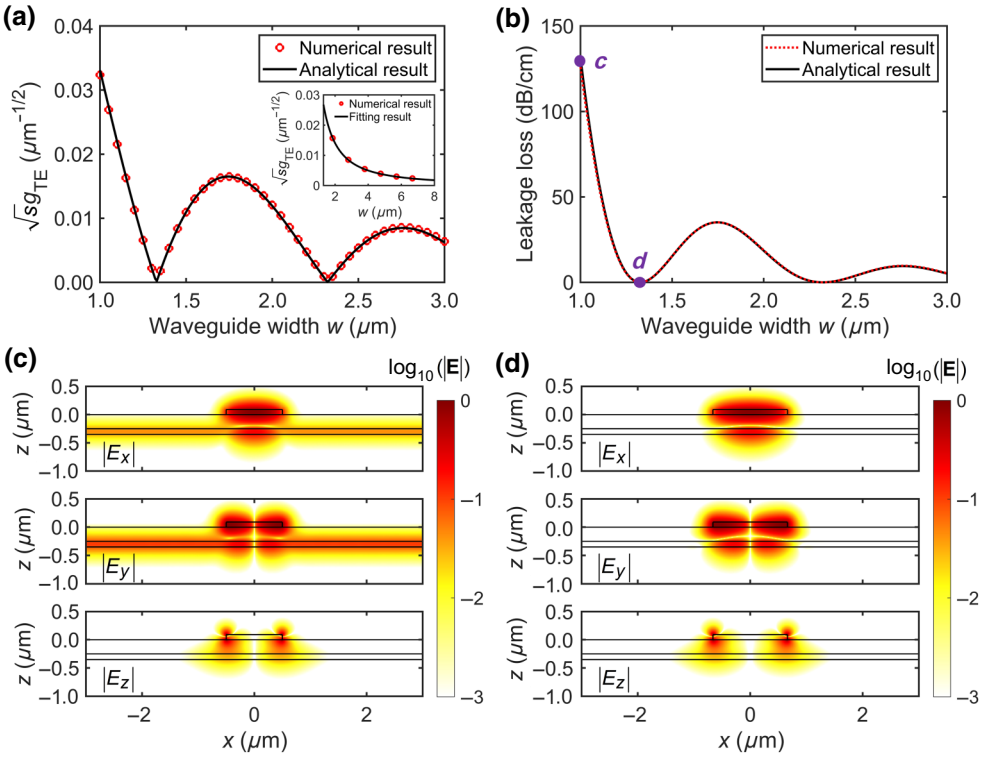

FIG. 3. Lateral leakage of bound surface mode in the TE continuum. (a) Normalized coupling strength between the TE bound surface mode and 21st TE discrete internal mode versus waveguide width w calculated by using both Eq. (3) (black solid line) and FDFD (red circles). Inset depicts normalized coupling strength versus waveguide width w at constructive interference condition [i.e., $(k_{\mathrm{TE},x}w + \varphi_{\mathrm{TE}})/\pi$ is even] and the fitting curve of $1/\sqrt{w^3}$. (b) Leakage loss of TE bound surface mode versus waveguide width w calculated by using both Eq. (6) (black solid line) and FDFD (red dotted line). Electric field distribution on $\log_{10}$ scale of (c) ordinary mode ($w = 1$ μm) and (d) BIC mode ($w = 1.325$ μm) indicated, respectively, by points c and d in (b). In calculations, thicknesses d_a and d_b are fixed at 250 and 100 nm, respectively.

can be expressed as

$$L_{\mathrm{TE}} = \frac{20}{\ln(10)} g_{\mathrm{TE}}^2 \rho_{\mathrm{TE}}, \tag{4}$$

where ρ_{TE} is the density of the TE continuum modes:

$$\rho_{\mathrm{TE}} \approx \frac{s n_{\mathrm{bound}}}{2\sqrt{n_{R1,\mathrm{int,TE}}^2 - n_{\mathrm{bound}}^2}}. \tag{5}$$

Substituting Eqs. (3) and (5) into Eq. (4), the leakage loss can be written as

$$L_{\mathrm{TE}} \approx \frac{10 c_{\mathrm{TE}}^2 \cos^2[(k_{\mathrm{TE},x} w + \varphi_{\mathrm{TE}})/2]}{\ln(10) w^3} \frac{n_{\mathrm{bound}}}{\sqrt{n_{\mathrm{R1,int,TE}}^2 - n_{\mathrm{bound}}^2}}. \tag{6}$$

As shown in Fig. 3(b), the leakage loss under varying waveguide widths is calculated analytically according to Eq. (6) (black solid line), which is in perfect coincidence with the numerical simulation by FDFD (red dotted line). Point d in Fig. 3(b) ($w = 1.325$ μm) indicates the BIC mode corresponding to zero leakage due to destructive interference. The BIC mode is corroborated intuitively by the electric field distribution, as shown in Fig. 3(d). As a comparison, Fig. 3(c) gives the electric field distribution corresponding to point c in Fig. 3(b) ($w = 1$ μm). It is clearly seen that the electromagnetic field of the BIC mode is well confined by the ridge without any leakage [Fig. 3(d)], while the ordinary guided mode leaks dramatically into the TE continuum mode within the substrate [Fig. 3(c)].

C. Lateral leakage of bound surface mode in both TE and TM continuums

Figure 4(a) shows the effective-refractive-index distribution of the waveguide on a single binary layer with $d_b = 146.5$ nm, in which the TE bound surface mode couples not only to the TE continuum but also to the TM continuum due to depolarization at the ridge corners (i.e., nonzero E_z). It is worth noting that the odd parity of electric field component E_z in the x direction [Fig. 2(c)] introduces an extra

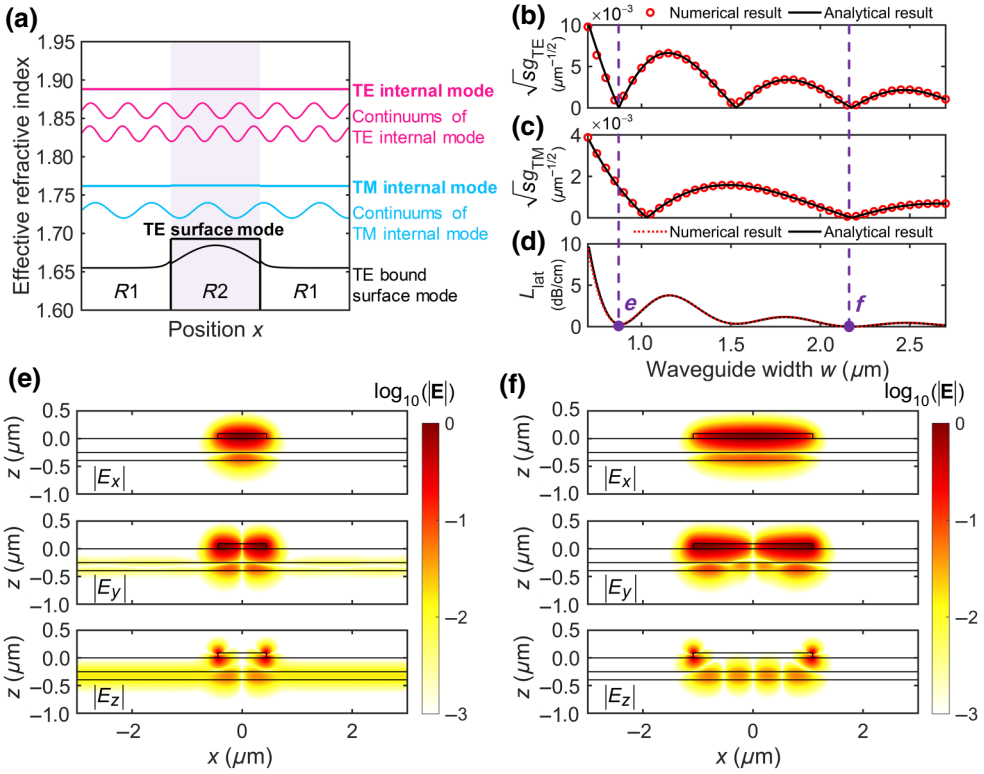

FIG. 4. Lateral leakage of bound surface mode in both TE and TM continuums. (a) Effective-refractive-index distribution of eigenmodes propagating along the y axis in a waveguide on a substrate of a single binary layer. Analytical and FDFD-calculated normalized coupling strength between the TE bound surface mode and (b) 21st TE discrete internal mode and (c) 16th TM discrete internal mode versus waveguide width w. (d) Leakage loss of TE bound surface mode versus waveguide width w calculated by using both Eq. (8) (black solid line) and FDFD (red dotted line). Electric field distribution on $\log_{10}$ scale of (e) quasi-BIC mode ($w = 0.88$ μm) and (f) BIC mode ($w = 2.17$ μm) indicated, respectively, by points e and f in (d). In calculations, thicknesses d_a and d_b are fixed at 250 and 146.5 nm, respectively.

π-phase difference between the left-going and right-going TM continuums. Hence, the coupling strength between the TE bound mode and the TM continuum (g_{TM}) can be written as

$$g_{TM} \approx c_{TM} \frac{|1 - e^{i(k_{TM,x}w + \varphi_{TM})}|}{2\sqrt{sw^3}}. \quad (7)$$

Figures 4(b) and 4(c) present the normalized coupling strengths, depending on the waveguide width, that are calculated analytically (black solid line) and simulated by FDFD (red circles) for TE bound mode-TE continuum coupling ($\sqrt{s}g_{TE}$) and TE bound mode-TM continuum coupling ($\sqrt{s}g_{TM}$), respectively. Although coupling between the modes under the same polarization is a little stronger, the coupling between the TE bound mode and the TM continuum cannot be ignored. Consequently, the leakage loss is caused by both TE and TM continuums:

$$L_{lat} = L_{TE} + L_{TM}. \quad (8)$$

Here, the loss caused by the TE continuum, L_{TE}, is given by Eq. (6) and the loss caused by the TM continuum, L_{TM}, can be expressed as

$$L_{TM} \approx \frac{10c_{TM}^2 \sin^2[(k_{TM,x}w + \varphi_{TM})/2]}{\ln(10)w^3} \times \frac{n_{bound}}{\sqrt{n_{R1,int,TM}^2 - n_{bound}^2}}. \quad (9)$$

Figure 4(d) shows the leakage loss as a function of the waveguide width calculated analytically by Eq. (8) (black solid line) and numerically by FDFD (red dotted line). Since the TE bound mode-TE continuum coupling dominates leakage loss, the loss curve presented in Fig. 4(d) has a similar profile to the curve of coupling strength drawn in Fig. 4(b), except for some details related to the BIC mode. Because the destructive interference is realized for the TE and TM continuums independently, the rigorous BIC mode is only obtained when $L_{TE} = 0$ and $L_{TM} = 0$ simultaneously, that is, $(k_{TE,x}w + \varphi_{TE})/\pi$ is odd and $(k_{TM,x}w + \varphi_{TM})/\pi$ is even. For instance, point f ($w = 2.17\ \mu$m) in Fig. 4(d) indicates a BIC mode, for which both TE and TM leakage are forbidden, and the electromagnetic field is well confined by the ridge waveguide [Fig. 4(f)]. However, the cancellation of TE or TM radiation commonly occurs under different ridge widths because of different wave vectors for the two orthogonal polarizations. Hence, leakage loss reaches nonzero minimums near the zero points of g_{TE}, leading to quasi-BIC modes with finite propagation length. The field distribution of the quasi-BIC mode indicated by point e in Fig. 4(d) ($w = 0.88\ \mu$m) is illustrated in Fig. 4(e), in which slight TM radiation can be observed when the main electromagnetic lobe is confined by the ridge.

IV. BSW WAVEGUIDE

A. Lateral leakage of bound BSW mode in the TE continuum

Figure 5(a) illustrates the BSW waveguide, which is composed of a Si_3N_4 ridge on top of a truncated 1DPC substrate. Compared with the bound surface mode discussed in Sec. III, the bound BSW mode is protected robustly by the PBG instead of TIR in the vertical direction, free from substrate impact. The continuous photonic band of the 1DPC is quantized to multiple internal modes because of truncation. If the bound BSW modes introduced by the ridge waveguide lie within the continuum of photonic bands, such as modes indicated by points a and b in Fig. 5(b), the coupling between them leads to

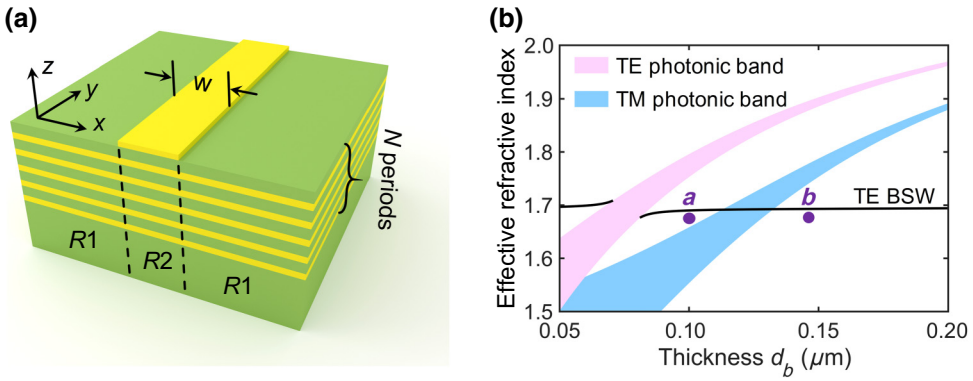

FIG. 5. Schematic of BSW waveguide and photonic band structure. (a) Schematic illustration of a BSW waveguide on multilayered substrate. (b) Photonic band structure of ideal 1DPC versus thickness d_b calculated by using TMM. Violet (blue) zone denotes zeroth TE (TM) photonic band, and white zone denotes PBG. Black solid line denotes TE BSW mode within region $R2$. TE bound BSW mode indicated by point a ($d_b = 100$ nm) lies on the TE continuum and that indicated by point b ($d_b = 146.5$ nm) lies on TE and TM continuums simultaneously. In calculations, thickness d_a is fixed at 250 nm.

leakage loss for the guided BSW mode. The coupling scenario for the BSW waveguide here is very similar to what happens in the waveguide based on a single binary layer, as discussed above, except that more intrinsic modes of the 1DPC substrate are involved. Considering the orthogonality among the TE internal modes in the TE photonic band, the entire leakage loss of the bound BSW mode is calculated by superposing the leakage loss to all involved leakage channels, which can be written as

$$L_{\mathrm{TE}} = \frac{20}{\ln(10)} \sum\nolimits_m (g_{\mathrm{TE}}^m)^2 \rho_{\mathrm{TE}}^m. \tag{10}$$

Here, the coupling strength,

$$g_{\mathrm{TE}}^m \approx c_{\mathrm{TE}}^m \frac{|1+e^{i(k_{\mathrm{TE},x}^m w+\varphi_{\mathrm{TE}})}|}{2\sqrt{sw^3}},$$

is in the same expression as Eq. (3), and

$$\rho_{\mathrm{TE}}^m \approx \frac{sn_{\mathrm{bound}}}{2\sqrt{(n_{R1,\mathrm{int,TE}}^m)^2 - n_{\mathrm{bound}}^2}}$$

is the density for the continuums of the mth TE internal mode, which is the same as that of Eq. (5). When N approaches infinity, the leakage loss is rewritten in the form of integration, $L_{\mathrm{TE}} = \frac{20}{\ln(10)} \int_{\mathrm{band}} (g_{\mathrm{TE}}^2 \rho_{\mathrm{int,TE}}) \rho_{\mathrm{TE}} dn_{\mathrm{eff}}$, where $\rho_{\mathrm{int,TE}}$ is the density of the TE internal modes.

Despite the same photonic band, leakage to different internal modes has variable contributions to loss because the coupling coefficient, c_{TE}^m, and the density of the TE internal modes, $\rho_{\mathrm{int,TE}}$, are quite different for every internal mode. As shown in Figs. 6(a)–6(c), the coupling coefficient, c_{TE}^m; the density of the TE internal mode, $\rho_{\mathrm{int,TE}}$; and the weight coefficient of $c_{\mathrm{TE}}^2 \rho_{\mathrm{int,TE}}$ are given for multilayered substrates with different layer pairs of $N = 1,\ 5,\ 10,\ 20,\ 500$, as calculated according to Eq. (2), by employing an approximation called the effective index method (EIM) [32]. The coupling coefficient and weight coefficient individually converge to a line approximately described by the numerical result of $N = 500$ as N approaches infinity. The leakage loss to the overall photonic band can be weighted by the coefficient $c_{\mathrm{TE}}^2 \rho_{\mathrm{int,TE}}$ without consideration of the BIC mechanism, and the profile of the weight coefficient is mainly determined by the coupling coefficient, c_{TE}^m. Although the density of TE internal modes, $\rho_{\mathrm{int,TE}}$, is significantly larger near the band edges [Fig. 6(b)], the total loss is mainly determined by loss to intermediate modes in the photonic band [Fig. 6(c)].

The most important effect introduced by the broad photonic band is derivation of the wave vectors, $k_{\mathrm{TE},x}^m$,

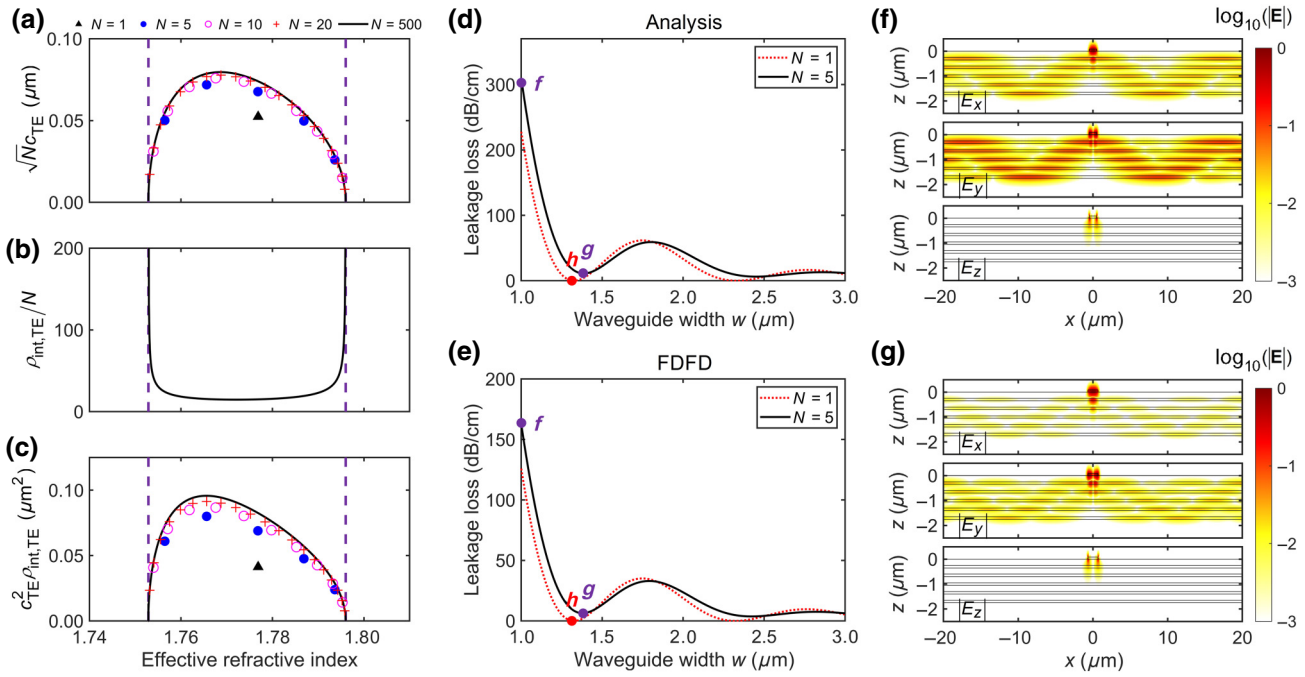

FIG. 6. Lateral leakage of bound BSW mode in the TE continuum. (a) Normalized coupling coefficient, (b) normalized density of TE internal modes, and (c) weight coefficient versus effective refractive index of internal modes. Violet dashed lines in (a)–(c) indicate edges of the zeroth TE photonic band. Leakage loss versus waveguide width w for waveguide on multilayered substrates of $N = 1,\ 5$, as calculated by using both (d) Eq. (10) and (e) FDFD. Electric field distribution on $\log_{10}$ scale of (f) ordinary mode ($w = 1\ \mu$m) and (g) quasi-BIC mode ($w = 1.38\ \mu$m) indicated, respectively, by points f and g in (d),(e). Point h in (d),(e) indicates BIC mode ($w = 1.325\ \mu$m) in the waveguide on the substrate of a single binary layer. In calculations, thicknesses d_a and d_b are fixed at 250 and 100 nm, respectively.

leading to the inconsistency of the BIC condition for different internal modes. Consequently, the leakage loss of the BSW waveguide can be suppressed but not eliminated completely. Figure 6(d) presents the analytical leakage loss of the BSW waveguide with $d_b = 100$ nm [point a in Fig. 5(b)], depending on the waveguide width calculated according to Eq. (10) (black solid line). The partially destructive interference causes the overall leakage to be suppressed under the BIC condition. In contrast to a BIC in the waveguide on a single binary layer (red dotted line), the minimum loss of the bound BSW mode is nonzero, leading to quasi-BICs, which is confirmed by the FDFD result shown in Fig. 6(e). It is notable that the peak position of the weight coefficient for the multilayer does not correspond to the effective refractive index of the single binary layer [triangle in Fig. 6(c)]. As a result, the waveguide width of the BSW waveguide for the quasi-BIC [e.g., point g in Figs. 6(d) and 6(e)] is slightly larger than that of the corresponding BIC in a waveguide on a single binary layer [e.g., point h in Figs. 6(d) and 6(e)].

Point g in Figs. 6(d) and 6(e) ($w = 1.38$ μm) indicates the quasi-BIC of a guided BSW, for which the majority of leakage is canceled out, owing to destructive interference [Fig. 6(g)]. The FDFD-calculated leakage loss of the quasi-BIC is as low as 6.41 dB/cm. As a comparison, Fig. 6(f) shows the electric field distribution of an ordinary guided mode, corresponding to point f in Figs. 6(d) and 6(e) ($w = 1$ μm), the leakage loss of which is remarkably large ($L_{TE} = 162.8$ dB/cm). As shown in Fig. 6(f), the leaky wave is a superposition of multiple TE internal modes, exhibiting the periodic field profile in the horizontal direction.

B. Low-loss bound BSW mode in both TE and TM continuums

Similar to the situation discussed in Sec. III C, the TE bound BSW mode lying in the continuum of both TE and TM photonic bands [point b in Fig. 5(b)] will leak into both continuums because of depolarization at the ridge corners. Figure 7(a) presents the leakage loss of the BSW waveguide with $d_b = 146.5$ nm [point b in Fig. 5(b)] under varying waveguide widths calculated by using FDFD. It is noticed that the leakage loss curve of the bound BSW mode ($N = 5$, black solid line) and the bound surface mode ($N = 1$, red dotted line) resemble each other somewhat in the profile, but the minimum leakage loss under the BIC condition is nonzero for the bound BSW mode because of multiple internal modes in the expanded photonic band. As shown in the inset violet box in Fig. 7(a), the quasi-BIC mode renders a very tiny leakage loss of 3.41×10^{-2} dB/cm [point g in the inset of Fig. 7(a)], which is 2 orders of magnitude lower than that of the quasi-BIC mode, as indicated by point g in Fig. 6(e).

As previously discussed, the bandwidth of the photonic band is a critical factor to diminish leakage loss of the quasi-BIC mode, which can be modified via varying the geometric parameters of the 1DPC. Figure 7(b) depicts the bandwidth of the zeroth TE and TM photonic bands under varying thicknesses of d_a and d_b. Increasing the thicknesses of either layer in the binary cell can narrow the photonic bands, and hence, benefits the degeneracy of the cancellation point for all internal modes in individual bands to achieve a low-loss quasi-BIC mode. Owing to the quasidegeneracy of multiple internal modes in the multilayered substrate of $d_b = 146.5$ nm, a low-loss bound BSW mode appears under the BIC condition [point g in the inset of Fig. 7(a)].

Therefore, a low-loss BSW waveguide can be designed in accordance with the following procedure. First, the simultaneous destructive interference of multiple orthogonal leakage channels (i.e., continuum of all participating TE and TM photonic bands) is a prerequisite, which is more sophisticated as the channel number increases; then, the multilayered substrate is designed with a narrow photonic band to enhance the degeneracy of cancellation

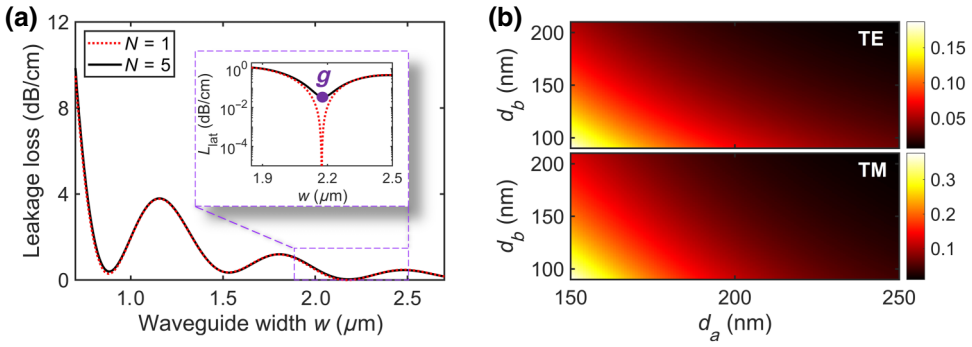

FIG. 7. Low-loss bound BSW mode in both TE and TM continuums. (a) Leakage loss versus waveguide width w for a waveguide on multilayered substrates of $N = 1$, 5 calculated by using FDFD, in which thicknesses d_a and d_b are fixed at 250 and 146.5 nm, respectively. Inset depicts $\log_{10}$-scale plot of the violet box, where point g indicates the low-loss bound BSW mode (quasi-BIC) with $w = 2.17$ μm. (b) Bandwidth of the zeroth TE (upper inset) and TM (lower inset) photonic bands versus thicknesses d_a and d_b calculated by using TMM.

points for all internal modes in individual bands, consolidating the elimination of leakage. Following this guidance, a BSW waveguide is designed with $d_a = 350$ nm, $d_b = 166$ nm, and $w = 0.801$ μm, for instance. The leakage loss of the low-loss bound BSW mode in this waveguide can be simulated to be as low as 3.79×10^{-5} dB/cm, which is significantly lower than the reported work with a loss of about 310 dB/cm [16].

V. BSW RESONATOR

A. Lateral leakage of BSW whispering gallery mode in both TE and TM continuums

Figure 8(a) schematically illustrates the proposed BSW resonator composed of a Si_3N_4 microdisk with radius R deposited on a multilayered substrate. The thickness of the disk is fixed at $h = 90$ nm in the following discussion. Similar to the leakage scenario of the BSW waveguide discussed above, the BSW whispering gallery mode (WGM) also inevitably couples to the cylindrical continuums within the substrate, causing lateral leakage and introducing an extra loss channel for the BSW resonator. The intrinsic loss of a conventional disk resonator generally consists of bending loss, material absorption, and scattering loss. Here, we neglect material absorption and scattering loss for the sake of simplicity, then the Q factor of the BSW resonator can be expressed as

$$\frac{1}{Q_{\mathrm{BSW}}} = \frac{1}{Q_{\mathrm{rad}}} + \frac{1}{Q_{\mathrm{lat}}}. \tag{11}$$

Here, the bending loss, Q_{rad}, represents leakage of the WGM into the freely propagating light wave and the lateral leakage, Q_{lat}, is related to the continuum mode of the multilayered substrate.

First, we investigate lateral leakage in the resonator on a substrate of a single binary layer. The WGM in such a resonator occurs when the TE surface electromagnetic wave circumnavigates around the edge of the Si_3N_4 disk [Fig. 8(b)]. The electric field of the TE surface WGM is localized near the edge of the disk, which can be expressed as $\mathbf{E} = \mathbf{E}(r,z)e^{iq\varphi}$ in the cylindrical coordinate (r,φ,z). Here, q is the azimuthal mode index denoting propagation. As shown in Fig. 8(c), the WGM dissipating to the continuums can be classified as an outer channel, t_{bc} (blue dashed line), and an inner channel, r_{bc} (red dashed line), with phase matching due to scattering at the disk edge

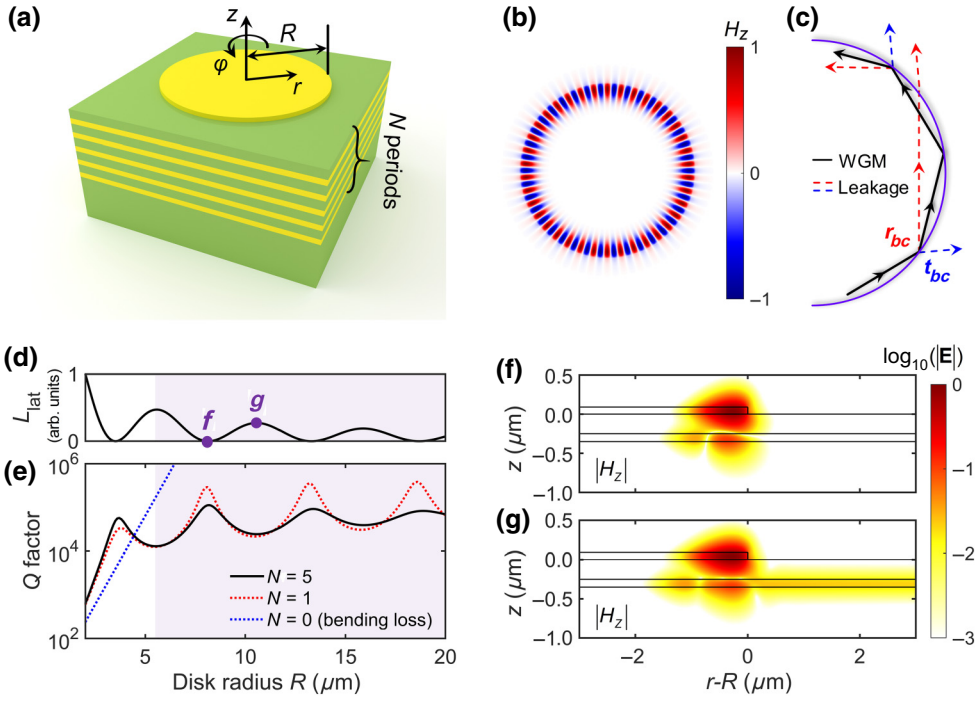

FIG. 8. Lateral leakage of BSW whispering gallery mode in both TE and TM continuums. (a) Schematic illustration of a BSW resonator on multilayered substrate. (b) Magnetic field distribution of TE surface WGM ($N = 1$) with $q = 38$ in Si_3N_4 disk. (c) Schematic illustration of WGM coupled to double-leakage channels in BSW resonator. (d) Analytical leakage loss of TE surface WGM versus disk radius, R, calculated by using Eq. (12). (e) Q factor versus disk radius, R, for a resonator on a substrate of homogeneous medium and multilayered substrates of $N = 1, 5$ calculated by using FDFD. Violet zone in (d),(e) indicates the radius range in which bending loss is over 1 order of magnitude lower than leakage loss. Magnetic field distribution on $\log_{10}$ scale for (f) quasi-BIC WGM ($R = 8.1$ μm) and (g) ordinary WGM ($R = 10.5$ μm) indicated, respectively, by points f and g in (d). In calculations, thicknesses d_a and d_b are fixed at 250 and 125 nm, respectively.

[33]. The leakage loss can be obtained from the amplitude of the leaky wave at the boundary of the disk, which is the coherent superposition of two leakage channels. Since the coupling between the TE WGM and the TE continuum is stronger than that between the TE WGM and the TM continuum, the leakage loss is dominated by the TE continuum [27]:

$$L_{\text{lat}} \propto J_q(n_{R1,\text{int,TE}} k_0 R)^2. \tag{12}$$

Here, $J_q(x)$ is the qth Bessel function. The criterion for the formation of the quasi-BIC mode is zero amplitude of TE leakage at the boundary of the disk, $J_q(n_{R1,\text{int,TE}} k_0 R) = 0$, which is achieved by destructive interference between two leakage channels.

The quasi-BIC WGM is illustrated by calculating the leakage loss of a resonator on a substrate of a single binary layer with geometric parameters of $d_a = 250$ nm and $d_b = 125$ nm. We focus on the radius range of $R > 5.5$ μm [violet zones in Figs. 8(d) and 8(e)], where the bending loss can be neglected (i.e., over 1 order of magnitude lower than the leakage loss). Figure 8(d) depicts the leakage loss calculated analytically by using Eq. (12), in which the leakage loss resonates and goes to zero quasiperiodically with respect to the disk radius. As shown in Fig. 8(e), the numerical Q factor calculated by FDFD (red dotted line) varies consistently with the analytical leakage loss, reaching maximums at zero points of leakage loss. The peak Q factor is determined by the slight loss arising from the TM lateral leakage, leading to quasi-BIC modes.

Point f in Fig. 8(d) ($R = 8.1$ μm) indicates the quasi-BIC mode, for which TE leakage is eliminated and the electromagnetic field is well confined by the disk [Fig. 8(f)]. On the contrary, Fig. 8(g) gives the magnetic field distribution corresponding to point g in Fig. 8(d) ($R = 10.5$ μm), in which the ordinary WGM exhibits significant leakage to the TE continuum within the substrate. Owing to the quasidegeneracy of multiple internal modes in the photonic band, quasiperiodic peaks of the Q factor still appear at proper radiuses that fulfill the BIC condition in the BSW resonator (black solid line), as shown in Fig. 8(e), validating that the BIC mechanism still works. Meanwhile, the valley and peak points of leakage loss related to multiple nondegenerate continuum modes are separate from each other, leading to a slight decrease for the peak values of the Q factor and an increase for the valley values compared with those of a resonator on a single binary layer.

B. High-Q BSW resonator

For the radius range of $R < 5.5$ μm [white zones in Figs. 8(d) and 8(e)], bending radiation and lateral leakage should be considered simultaneously because they are comparable in intensity. An intriguing phenomenon can be observed in Fig. 8(e) that the Q factor of the BSW resonator is enhanced compared with that of a conventional resonator ($N = 0$) within the radius range of $R < 4.4$ μm, even though it has one more loss channel. Since the parity of the electromagnetic field in adjacent layer pairs for the TE BSW within the first PBG is odd, the initial field of bending radiations occurring at adjacent layer pairs are opposite in sign and different in amplitude, and then they have partially destructive interference in the field-overlap region, which suppresses bending loss and results in an enhancement of the overall Q factor. To interpret this phenomenon intuitively, the electric field distribution of the TE WGM in resonators with $R = 4$ μm are depicted, based on the substrate of a homogeneous medium [Fig. 9(a)] and multilayered substrates [Figs. 9(b) and 9(c)] for which the BIC condition is satisfied. Lateral leakage in the last two vanishes owing to the BIC mechanism. Moreover, compared with the conventional resonator [Fig. 9(a)], bending radiation is significantly weaker in the resonator on a single binary layer [Fig. 9(b)] and further down in the BSW resonator [Fig. 9(c)], which clearly validates the suppression of bending loss.

To obtain a high-Q BSW resonator, the two loss channels, with essentially different mechanisms, should be considered comprehensively. For a resonator with a fixed radius, the geometric parameters of a multilayered substrate are key parameters to optimize to maximize the overall Q factor. The thickness d_b is adjusted to enable the effective refractive index of the photonic band to satisfy the BIC condition [Eq. (12)] to guarantee that the Q factor is nearly at a maximum. Then, the thickness d_a is adjusted to an appropriate value that equilibrates bending loss and leakage loss to maximize the peak value, realizing a considerable Q factor. Hence, scanning of the geometric parameters of the multilayer is performed to obtain the optimal parameters. For instance, Fig. 9(d) presents the scanning result for the BSW resonator with $R = 4$ μm. A sharp peak of the Q factor formed under varying thicknesses of d_b can be observed in Fig. 9(d), corresponding to the BIC mechanism. The maximum Q factor ($Q_{\text{BSW}} = 1.9 \times 10^5$) is obtained at the black circle in Fig. 9(d) (i.e., $d_a = 276$ nm, $d_b = 119$ nm), rendering a Q-factor enhancement of 12.8 dB with respect to that of the corresponding conventional resonator ($Q_C = 9.96 \times 10^3$). Furthermore, scanning is performed for the BSW resonator under varying radiuses. As shown in Fig. 9(e), the Q factor remains enhanced in the optimized BSW resonator within a wide range of radiuses.

Another important parameter that measures the performance of the resonator is the Purcell factor [$F = (3/4\pi^2)(Q/V)(\lambda/n_b)^3$], which determines the enhancement of emission mediated by the resonator. Here, V is the effective mode volume. For instance, the effective mode volume of the optimized BSW resonator with $R = 4$ μm is simulated to be $V_{\text{BSW}} = 0.3608$ μm^3, which is approximately equal to that of the corresponding conventional resonator

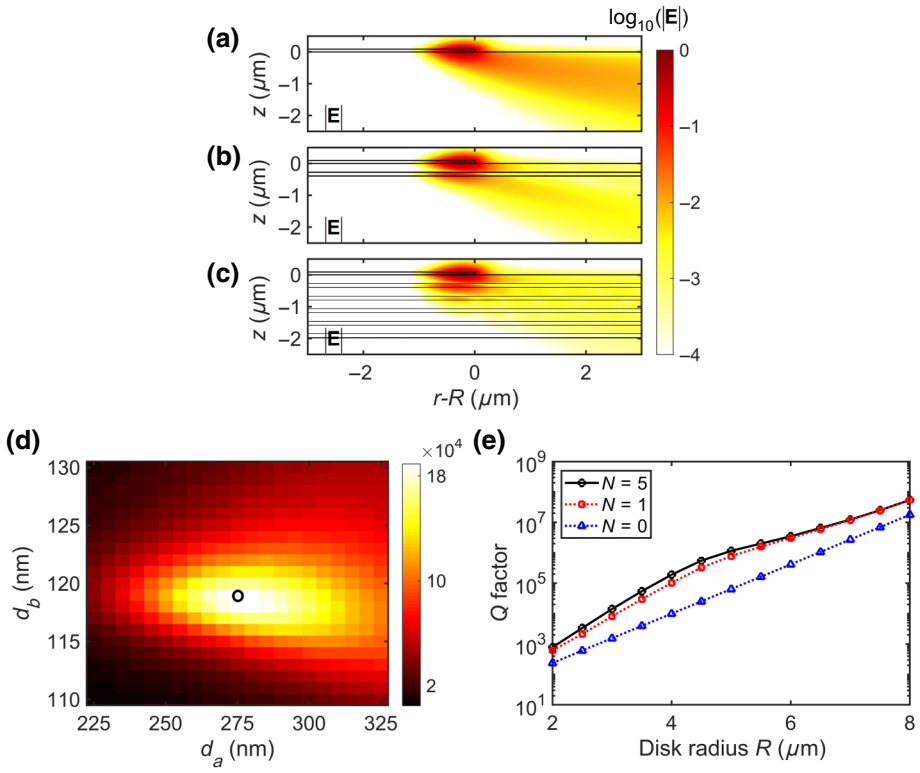

FIG. 9. High-Q BSW resonator. Electric field distribution on $\log_{10}$ scale of TE WGM in the resonator with $R = 4\ \mu$m based on (a) substrate of homogeneous medium and optimized multilayered substrates [indicated by black circle in (d)] of (b) $N = 1$ and (c) $N = 5$. (d) Q factor of BSW resonator ($N = 5$) with $R = 4\ \mu$m versus thicknesses d_a and d_b calculated by using FDFD. Black circle in (d) indicates the optimal geometric parameter of the multilayered substrate (i.e.,$d_a = 276$ nm, $d_b = 119$ nm), where the overall Q factor reaches a maximum. (e) FDFD-calculated Q factor versus disk radius, R, for a resonator on a substrate of homogeneous medium and that on multilayered substrates of $N = 1, 5$ optimized for each radius individually.

($V_C = 0.3664\ \mu\text{m}^3$). Owing to the considerable Q-factor enhancement, the Purcell factor of the optimized BSW resonator is significantly large, $F_{\text{BSW}} = 614.8$, and about 19 times larger than that of the corresponding conventional resonator ($F_C = 31.7$).

VI. CONCLUSION

We investigate the lateral leakage loss arising from coupling between the bound surface mode and the continuums within the truncated 1DPC. For the waveguide on a single-binary-layer substrate, lateral leakage can be eliminated by elaborate design due to the simultaneous destructive interference of TE and TM continuums, realizing a BIC mode with an infinite propagation length. Only a quasi-BIC mode can be obtained in the BSW waveguide, owing to the narrow broadening of the photonic band, realizing a low-loss BSW waveguide with an intrinsic propagation loss of 3.79×10^{-5} dB/cm. The BSW resonator is optimized to maximize the Q factor under the comprehensive consideration of both bending loss and lateral leakage, realizing an enhancement of 12.8 dB for both the Q factor and the Purcell factor, with respect to that of the corresponding conventional resonator. We believe that this work will provide guidance on constructing PICs on a BSW platform; such a platform will benefit many chip-scale optical applications in lasing, sensing, nonlinear optics, optical switches, and optical networks.

ACKNOWLEDGMENTS

This work is supported by the National Natural Science Foundation of China (Grants No. U20A20216 and No. 11674303), the National Key R&D Program of China (Grant No. 2020YFB2007501), and Anhui Provincial Science and Technology Major Projects (Grant No. 18030901005). P.W. is also supported by the Advanced Laser Technology Laboratory of Anhui Province under Grant No. 20191004.

[1] H. Rong, S. Xu, O. Cohen, O. Raday, M. Lee, V. Sih, and M. Paniccia, A cascaded silicon Raman laser, Nat. Photonics **2**, 170 (2008).

[2] B. Morrison, A. Casas-Bedoya, G. Ren, K. Vu, Y. Liu, A. Zarifi, T. G. Nguyen, D.-Y. Choi, D. Marpaung, S. J. Madden, A. Mitchell, and B. J. Eggleton, Compact Brillouin devices through hybrid integration on silicon, Optica **4**, 847 (2017).

[3] D. J. Moss, R. Morandotti, A. L. Gaeta, and M. Lipson, New CMOS-compatible platforms based on silicon nitride and Hydex for nonlinear optics, Nat. Photonics **7**, 597 (2013).

[4] R. Salem, M. A. Foster, A. C. Turner, D. F. Geraghty, M. Lipson, and A. L. Gaeta, Signal regeneration using low-power four-wave mixing on silicon chip, Nat. Photonics **2**, 35 (2007).

[5] C. Wang, M. Zhang, X. Chen, M. Bertrand, A. Shams-Ansari, S. Chandrasekhar, P. Winzer, and M. Loncar, Integrated lithium niobate electro-optic modulators

operating at CMOS-compatible voltages, Nature **562**, 101 (2018).
[6] I. Datta, S. H. Chae, G. R. Bhatt, M. A. Tadayon, B. Li, Y. Yu, C. Park, J. Park, L. Cao, D. N. Basov, J. Hone, and M. Lipson, Low-loss composite photonic platform based on 2D semiconductor monolayers, Nat. Photonics **14**, 256 (2020).
[7] J. Leuthold, C. Koos, and W. Freude, Nonlinear silicon photonics, Nat. Photonics **4**, 535 (2010).
[8] S. I. Bozhevolnyi, V. S. Volkov, E. Devaux, J.-Y. Laluet, and T. W. Ebbesen, Channel plasmon subwavelength waveguide components including interferometers and ring resonators, Nature **440**, 508 (2006).
[9] W. L. Barnes, A. Dereux, and T. W. Ebbesen, Surface plasmon subwavelength optics, Nature **424**, 824 (2003).
[10] P. Yeh, A. Yariv, and C. S. Hong, Electromagnetic propagation in periodic stratified media. I. General theory, J. Opt. Soc. Am. **67**, 423 (1977).
[11] R. D. Meade, K. D. Brommer, A. M. Rappe, and J. Joannopoulos, Electromagnetic Bloch waves at the surface of a photonic crystal, Phys. Rev. B **44**, 10961 (1991).
[12] D. Aurelio and M. Liscidini, Electromagnetic field enhancement in Bloch surface waves, Phys. Rev. B **96**, 045308 (2017).
[13] R. Badugu, K. Nowaczyk, E. Descrovi, and J. R. Lakowicz, Radiative decay engineering 6: Fluorescence on one-dimensional photonic crystals, Anal. Biochem. **442**, 83 (2013).
[14] A. Sinibaldi, N. Danz, E. Descrovi, P. Munzert, U. Schulz, F. Sonntag, L. Dominici, and F. Michelotti, Direct comparison of the performance of Bloch surface wave and surface plasmon polariton sensors, Sens. Actuators B **174**, 292 (2012).
[15] E. Descrovi, T. Sfez, M. Quaglio, D. Brunazzo, L. Dominici, F. Michelotti, H. P. Herzig, O. J. Martin, and F. Giorgis, Guided Bloch surface waves on ultrathin polymeric ridges, Nano Lett. **10**, 2087 (2010).
[16] R. Wang, H. Xia, D. Zhang, J. Chen, L. Zhu, Y. Wang, E. Yang, T. Zang, X. Wen, G. Zou, P. Wang, H. Ming, R. Badugu, and J. R. Lakowicz, Bloch surface waves confined in one dimension with a single polymeric nanofibre, Nat. Commun. **8**, 14330 (2017).
[17] B. Vosoughi Lahijani, H. Badri Ghavifekr, R. Dubey, M. S. Kim, I. Vartiainen, M. Roussey, and H. P. Herzig, Experimental demonstration of critical coupling of whispering gallery mode cavities on a Bloch surface wave platform, Opt. Lett. **42**, 5137 (2017).
[18] S. Longhi, Quantum-optical analogies using photonic structures, Laser Photon. Rev. **3**, 243 (2009).
[19] C. W. Hsu, B. Zhen, A. D. Stone, J. D. Joannopoulos, and M. Soljačić, Bound states in the continuum, Nat. Rev. Mater. **1**, 16048 (2016).
[20] J. von Neumann and E. Wigner, On some peculiar discrete eigenvalues, Phys. Z. **30**, 465 (1929).
[21] Y. Plotnik, O. Peleg, F. Dreisow, M. Heinrich, S. Nolte, A. Szameit, and M. Segev, Experimental Observation of Optical Bound States in the Continuum, Phys. Rev. Lett. **107**, 183901 (2011).
[22] J. Chen and P. Chu, Phase-induced Fano antiresonance in a planar waveguide with two dielectric ridges, J. Opt. Soc. Am. B **36**, 3417 (2019).
[23] C. W. Hsu, B. Zhen, S.-L. Chua, S. G. Johnson, J. D. Joannopoulos, and M. Soljacic, Bloch surface eigenstates within the radiation continuum, Light Sci. Appl. **2**, e84 (2013).
[24] S.-G. Lee, S.-H. Kim, and C.-S. Kee, Bound states in the continuum (BIC) accompanied by avoided crossings in leaky-mode photonic lattices, Nanophotonics **9**, 4373 (2020).
[25] S. I. Azzam, V. M. Shalaev, A. Boltasseva, and A. V. Kildishev, Formation of Bound States in the Continuum in Hybrid Plasmonic-Photonic Systems, Phys. Rev. Lett. **121**, 253901 (2018).
[26] X. Gao, B. Zhen, M. Soljačić, H. Chen, and C. W. Hsu, Bound states in the continuum in fiber bragg gratings, ACS Photon. **6**, 2996 (2019).
[27] C.-L. Zou, J.-M. Cui, F.-W. Sun, X. Xiong, X.-B. Zou, Z.-F. Han, and G.-C. Guo, Guiding light through optical bound states in the continuum for ultrahigh-Q microresonators, Laser Photon. Rev. **9**, 114 (2015).
[28] X. Lei, Y. Ren, Y. Lu, and P. Wang, Lens for Efficient Focusing of Bloch Surface Waves, Phys. Rev. Appl. **10**, 044032 (2018).
[29] C.-L. Zou, X.-D. Chen, X. Xiong, F.-W. Sun, X.-B. Zou, Z.-F. Han, and G.-C. Guo, Photonic simulation of system-environment interaction: Non-markovian processes and dynamical decoupling, Phys. Rev. A **88**, 063806 (2013).
[30] Ansys Lumerical Inc., https://www.lumerical.com/products/mode/.
[31] J. Chen, D. Zhang, P. Wang, H. Ming, and J. R. Lakowicz, Strong Polarization Transformation of Bloch Surface Waves, Phys. Rev. Appl. **9**, 024008 (2018).
[32] M. Liscidini, Surface guided modes in photonic crystal ridges: The good, the bad, and the ugly, J. Opt. Soc. Am. B **29**, 2103 (2012).
[33] T. G. Nguyen, R. S. Tummidi, T. L. Koch, and A. Mitchell, Lateral leakage in TM-like whispering gallery mode of thin-ridge silicon-on-insulator disk resonators, Opt. Lett. **34**, 980 (2009).